

Discovery of Furanone-Based Radiopharmaceuticals for Diagnostic Targeting of COX-1 in Ovarian Cancer

Md. Jashim Uddin,^{*,†,‡,§,¶} Andrew J. Wilson,[‡] Brenda C. Crews,[†] Paola Malerba,^{†,§} Md. Imam Uddin,^{||,¶} Philip J. Kingsley,[†] Kebreab Ghebreselasie,[†] Cristina K. Daniel,[†] Michael L. Nickels,[⊥] Mohammed N. Tantawy,[⊥] Elma Jashim,^{†,¶} H. Charles Manning,^{⊥,¶} Dineo Khabele,^{‡,¶} and Lawrence J. Marnett^{*,†,‡,¶}

[†]A. B. Hancock, Jr., Memorial Laboratory for Cancer Research, Department of Biochemistry, Chemistry and Pharmacology, Vanderbilt Institute of Chemical Biology, Vanderbilt-Ingram Cancer Center, and [⊥]Department of Radiology and Radiological Sciences, Vanderbilt Institute of Imaging Sciences, Vanderbilt University School of Medicine, Nashville, Tennessee 37232, United States

[‡]Department of Obstetrics & Gynecology, Women's Reproductive Health Research Center, and ^{||}Department of Ophthalmology and Visual Sciences, Vanderbilt Eye Institute, Vanderbilt University Medical Center, Nashville, Tennessee 37232, United States

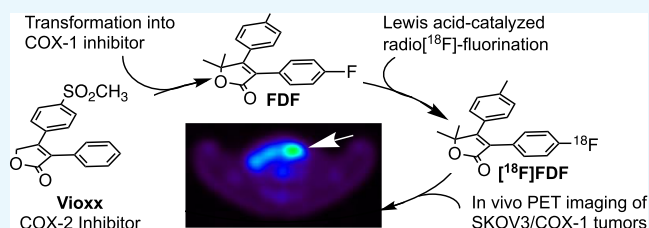
[§]Department of Pharmacy & Pharmaceutical Sciences, University of Bari "A. Moro", Via Orabona 4, 70125 Bari, Italy

[#]Martin Luther King Jr. Academic Magnet School of Health Sciences and Engineering, 613 17th Avenue North, Nashville, Tennessee 37203, United States

[¶]Department of Obstetrics and Gynecology, University of Kansas School of Medicine, Kansas City, Kansas 66160, United States

Supporting Information

ABSTRACT: In vivo targeting and visualization of cyclooxygenase-1 (COX-1) using multimodal positron emission tomography/computed tomography imaging represents a unique opportunity for early detection and/or therapeutic evaluation of ovarian cancer because overexpression of COX-1 has been characterized as a pathologic hallmark of the initiation and progression of this disease. The furanone core is a common building block of many synthetic and natural products that exhibit a wide range of biological activities. We hypothesize that furanone-based COX-1 inhibitors can be designed as imaging agents for the early detection, delineation of tumor margin, and evaluation of treatment response of ovarian cancer. We report the discovery of 3-(4-fluorophenyl)-5,5-dimethyl-4-(*p*-tolyl)furan-2(*5H*)-one (FDF), a furanone-based novel COX-1-selective inhibitor that exhibits adequate in vivo stability, plasma half-life, and pharmacokinetic properties for use as an imaging agent. We describe a novel synthetic scheme in which a Lewis acid-catalyzed nucleophilic aromatic deiodo[¹⁸F]fluorination reaction is utilized for the radiosynthesis of [¹⁸F]FDF. [¹⁸F]FDF binds efficiently to COX-1 in vivo and enables sensitive detection of ovarian cancer in subcutaneous and peritoneal xenograft models in mice. These results provide the proof of principle for COX-1-targeted imaging of ovarian cancer and identify [¹⁸F]FDF as a promising lead compound for further preclinical and clinical development.



INTRODUCTION

Ovarian cancer is the fifth most common cause of cancer death in women in the United States¹ due in large part to the fact that it is difficult to detect at an early stage.² Thus, although treatment of epithelial ovarian cancer has a high success rate if the disease is detected early,³ most women present with a pelvic mass reflecting advanced disease that is associated with a poor prognosis.⁴ Better imaging modalities are surely needed for early detection,⁵ presurgical evaluation,⁶ and therapeutic monitoring of ovarian cancer in patients.⁷ To meet these needs, [¹⁸F]FDG-positron emission tomography (PET) has been evaluated for the diagnosis and treatment of ovarian cancer in a number of clinical studies,⁸ but it has not demonstrated adequate specificity or sensitivity.⁹ [¹⁸F]FDG-

PET combined with computerized tomography (CT) ([¹⁸F]FDG-PET/CT) exhibits greater specificity but still lacks adequate sensitivity.¹⁰ Other PET molecular imaging agents have shown some promise in animal models of ovarian cancer, but none has yet progressed to the clinic.^{11–13} Clearly, the availability of a targeted ¹⁸F-labeled PET imaging agent that is effective for early diagnosis of ovarian cancer would be a major advance in the fight against this disease.¹⁴

Emerging preclinical and clinical evidence suggests that the enzyme cyclooxygenase-1 (COX-1) is an important contrib-

Received: April 16, 2019

Accepted: May 9, 2019

Published: May 24, 2019

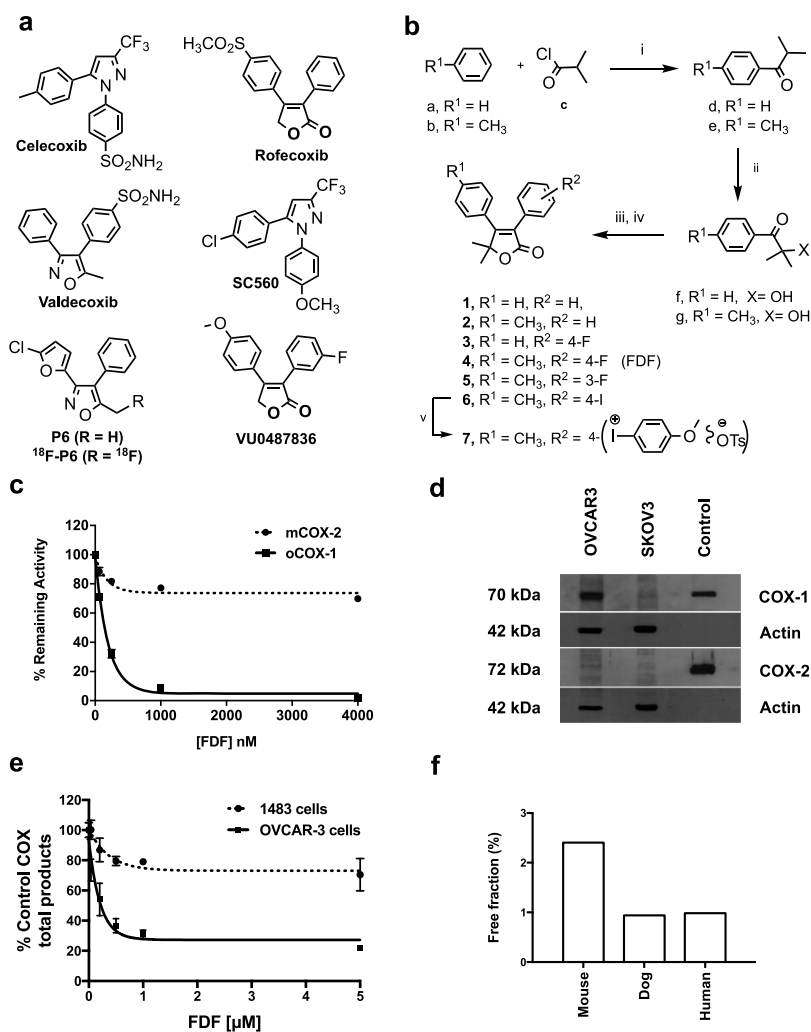


Figure 1. (a) Structure of COX-2-selective inhibitors (celecoxib, rofecoxib, and valdecoxib) and COX-1-selective inhibitors (SC560, P6/¹⁸F-P6, and VU0487836). (b) Chemical synthesis of FDF and analogs, (i) AlCl₃, CHCl₃, 0–25 °C, 1.5 h, (ii) trioctylmethylammonium chloride (Aliquat 336), NaOH, CCl₄, toluene, 25 °C, 16 h, (iii) substituted-phenylacetic acid, CMC, 4-(dimethylamino)pyridine, CH₂Cl₂, 25 °C, 18 h, (iv) DBU, 40–50 °C, 3 h, (v) anisole, *m*-CPBA, *p*-TSrt 16 h. (c) Inhibition of purified ovine COX-1 or mouse COX-2 by compound 4 (FDF). (d) Levels of COX-1 and COX-2 expression in OVCAR3, and SKOV3 cells by western blot analysis (cropped gels are displayed) using ovine COX-1 antibody (Santa Cruz# SC-19998) and human COX-2 antibody (Cayman# 100034), the full-length gels are presented in Supporting Figure S29, (e) inhibition of COX-1 and COX-2 in OVCAR3 and 1483 HNSCC cells by FDF. (f) Plasma protein binding of FDF in mouse, dog, and human.

utor to the early growth of ovarian cancer.^{15–17} This characteristic distinguishes ovarian cancer from most other malignancies, in which the second cyclooxygenase isoform, COX-2, is expressed early in tumorigenesis and helps to drive disease progression.¹⁸ COX-1 and COX-2 catalyze the rate-limiting step in prostaglandin (PG) and thromboxane (TX) biosynthesis—the oxygenation of polyunsaturated fatty acids to PG endoperoxides.¹⁹ PGs and TX contribute to tumor cell proliferation, resistance to apoptosis, migration, and angiogenesis.²⁰ COX-1 and COX-2 are the primary targets of nonsteroidal anti-inflammatory drugs (NSAIDs), which may account for the ability of NSAIDs to slow the progression of many forms of cancer.²¹ The exact role of COX-1 in ovarian cancer pathogenesis remains to be determined; however, its unique pattern of expression in ovarian malignancies leads to the hypothesis that COX-1 can serve as a novel target for molecular imaging probes to be used for early detection, presurgical evaluation, and monitoring the response to treatment of this elusive disease.²² To test this hypothesis, we developed a radiofluorinated analog of P6 (Figure 1a), a

known COX-1-selective inhibitor (COX-1 IC₅₀ = 1.9 μM, COX-2 IC₅₀ > 4 μM). In mice, distribution data showed higher [¹⁸F]P6 uptake in human OVCAR3 ovarian cancer xenografts than in the surrounding leg muscle, but the amount of radioactivity in the tumor was not sufficient to enable microPET/CT visualization.²³ This result suggested that it is possible to develop a COX-1-targeted PET agent, but that a successful compound should be at least 10-fold more effective than [¹⁸F]P6 as a COX-1 inhibitor. Also, in contrast to [¹⁸F]P6, in which ¹⁸F was incorporated as a fluoromethyl group, the ideal COX-1-targeted agent should contain ¹⁸F in a metabolically stable position (e.g., on an aromatic ring).

Herein, we report the discovery of 3-(4-fluorophenyl)-5,5-dimethyl-4-(*p*-tolyl)furan-2(*5H*)-one (FDF), a COX-1-selective inhibitor optimized from a series of furanone-based biologically active organic compounds, and we provide a novel acid-catalyzed iodonium chemistry scheme for its radiofluorination. We describe the utility and validation of [¹⁸F]FDF in COX-1-targeted imaging of ovarian cancer in

mouse models of subcutaneous and peritoneal tumors by PET/CT.

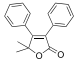
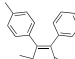
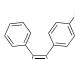
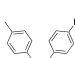
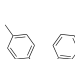
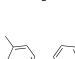
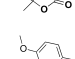
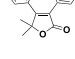
RESULTS

Chemical Synthesis. The majority of both COX-1- and COX-2-selective inhibitors has been based on a diarylheterocycle scaffold (Figure 1a). Our first attempt to discover fluorinated COX-1-selective inhibitors with higher potency than ^{18}F -P6 resulted in VU0487836, based on the furanone scaffold of the diarylheterocycle, rofecoxib. Attempts to incorporate ^{18}F into this molecule under conditions typically used for radiosynthesis failed, however, presumably because of the instability of the furanone ring. We hypothesized that incorporation of a 5,5-dimethyl group into the furanone ring would stabilize the molecule. Thus, we developed a synthetic scheme for analogs of VU0487836 bearing this substituent beginning with the synthesis of arylalkyl ketones (d,e) using a Friedel–Crafts acylation reaction between substituted-arenes (a,b) and acyl chloride (c) (Figure 1b). In this electrophilic aromatic substitution reaction, a stoichiometric amount of a Lewis acid catalyst, AlCl_3 , was used to prevent a second substitution on the aromatic rings. The α -hydroxylation of ketones (d,e) was carried out in an immiscible heterogeneous system containing NaOH, alkylaryl-ketones, and Aliquat 336, a lipophilic quaternary ammonium salt as a phase-transfer catalyst. Aliquat 336 was utilized to extract and transfer OH^- anions to the organic phase of the biphasic system for efficient reaction to afford hydroxy ketones (f,g). A one-pot procedure was employed for the synthesis of 5,5-dimethyl-furanones (1–6). First, substituted-phenylacetic acids were reacted with hydroxyl compounds to generate the corresponding esters *in situ*. The esters were then cyclized intramolecularly in the presence of 1,8-diazabicyclo[5.4.0]undec-7-ene (DBU) to afford the furanone products 1–6. The iodo-compound 6 was treated with anisole in the presence of *m*-chloroperbenzoic acid (*m*-CPBA) and *p*-toluenesulfonic acid to afford compound 7 (Figure 1b).

Inhibition of Purified Cyclooxygenases. Inhibition of purified ovine COX-1 or mouse COX-2 by test compounds 1–7 was assessed using a previously described method²⁴ that quantifies the conversion of [$1\text{-}^{14}\text{C}$]arachidonic acid to [$1\text{-}^{14}\text{C}$]PG products. The IC_{50} values for inhibition of purified human COX-2 or ovine COX-1 by test compounds (1–7) are summarized in Table 1. 5,5-Dimethyl-3,4-diphenylfuranone (1) displayed selective COX-1 inhibition with no inhibition of COX-2 at concentrations up to 25 μM . Incorporation of a methyl group at the para-position of the C-4 phenyl ring led to compound 2, which exhibited a significant increase in potency with retained selectivity against COX-1. As a fluoro-functionality is required for ^{18}F -PET imaging, compounds 3, 4, and 5 were synthesized. Of the three, compound 5 was the most potent, but also the least selective. Compound 4 (FDF) exhibited the best combination of potency and selectivity (Figure 1c). Replacement of the fluoro-group of FDF by an iodo substituent afforded 6, which retained potent and selective COX-1 inhibition. Compound 7, an iodonium tosylate salt required as a radiofluorination precursor, failed to inhibit either of the COX isoforms.

Levels of Cyclooxygenases in Cells. We and others previously reported that the SKOV3/COX-1 human ovarian adenocarcinoma cell line expresses high levels of COX-1 but does not express COX-2, whereas SKOV3/pcDNA cells do not express any of the COX isoforms.^{22,25,26} Here, we evaluated

Table 1. In Vitro Biochemical Properties of Furanone Derivatives 1–7 and Rofecoxib

Compound Nos.	Chemical Structure	Purified COX Isozymes		OVCAR Cells	HNSCC Cells
		IC_{50} (μM)		IC_{50} (μM)	IC_{50} (μM)
		COX-1	COX-2	COX-1	COX-2
1		0.36	> 25	0.12	> 5
2		0.05	> 25	0.49	> 5
3		0.64	> 25	0.28	> 5
4 (FDF)		0.14	> 25	0.22	> 5
5		0.05	4.00	0.13	> 5
6		0.04	> 25	0.80	> 5
7		> 25	> 25	> 5	> 5
Rofecoxib		> 25	0.14	> 5	0.03

the expression of both COX-1 and COX-2 in the SKOV3, and OVCAR3 ovarian cancer cell lines by western blot analysis using commercially available specific antibodies. Purified COX-1 and COX-2 served as standards, and actin was used as a loading control. The data revealed that COX-1 was expressed strongly in OVCAR3 cells and weakly in SKOV3 cells, and none of these cell lines expresses COX-2 enzyme (Figure 1d). Thus, these cells including SKOV3/COX-1, 1483 HNSCC, and SKOV3/pcDNA should be useful to evaluate the selectivity and potency of compounds 1–7 in the cellular and/or *in vivo* settings.

Inhibition of Cyclooxygenases in Cells. We evaluated the ability of compounds 1–7 to inhibit COX-1 in intact OVCAR3 cells and COX-2 in 1483 HNSCC cells (data for FDF are shown in Figure 1e).²⁴ Compounds 1–6 all exhibited potent and selective COX-1 inhibition in these assays, whereas compound 7 was inactive (Table 1). Because of its combined potency and selectivity in both the purified protein and cell-based assays, we considered FDF to be the most promising compound in the series.

Optimization by Radiomimetic Chemistry. To optimize conditions for radiosynthesis of [^{18}F]FDF, we first carried out the planned reaction using ^{19}F -containing reagents. We synthesized the iodonium precursor by reacting its iodo-

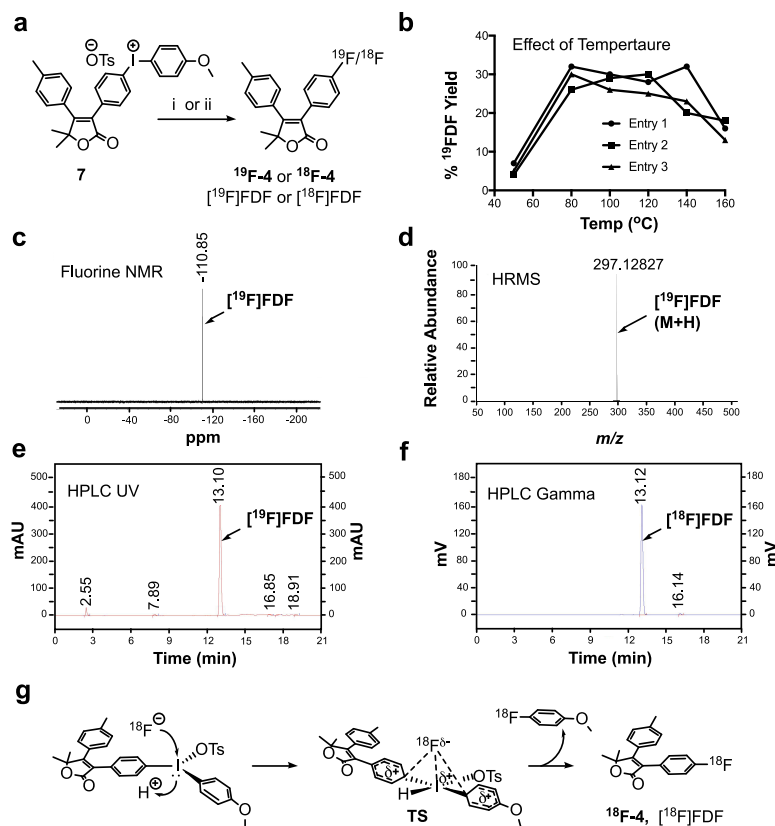


Figure 2. (a) Scheme for radiomimetic chemistry or radiochemistry, (i) ^{19}F - Bu_4NF , *m*-CPBA, DMSO, 80 °C, 30 min. (ii) Bu_4NHCO_3 , ^{18}F -fluoride, *m*-CPBA, DMSO, 80 °C, 30 min. (b) Effect of temperature on the deiodofluorination reaction. (c) Fluorine NMR spectrum of ^{19}F FDF. (d) HRMS spectrum of ^{19}F FDF. (e) HPLC UV chromatogram of ^{18}F FDF. (f) Radio-HPLC (HPLC gamma) chromatogram of ^{18}F FDF. (g) Proposed mechanism of acid-catalysis in novel deiodo ^{18}F fluorination reaction.

derivative (7) with anisole in the presence of *m*-chloroperoxybenzoic acid (*m*-CPBA) and *p*-toluenesulfonic acid. This procedure was robust and high-yielding. For incorporation of ^{19}F -fluorine, we initially reacted the iodonium salt with ^{19}F tetrabutylammonium fluoride (TBAF)/dimethyl sulfoxide (DMSO) at 80 °C for 30 min. This route occasionally afforded the desired ^{19}F FDF, but with very low yields (~1%). The failure led us to investigate a number of alternative approaches, including K^{19}F /Kryptofix2.2.2/ Cs_2CO_3 /*N,N*-dimethylformamide (DMF) at 80 °C for 10 min, K^{19}F /Kryptofix2.2.2/ K_2CO_3 /2,2,6,6-tetramethylpiperidine-1-oxyl (TEMPO)/DMF at 110 °C for 30 min, or ^{19}F KF/Kryptofix2.2.2/TEMPO/ CH_3CN at 80 °C for 10 min. Unfortunately, none of these reactions afforded the desired ^{19}F FDF product. Then, we reacted the iodonium salt with ^{19}F TBAF/DMSO in the presence of *m*-CPBA for 30 min at 80 °C, which afforded ^{19}F FDF in 33% yield (Figure 2a). We evaluated the effect of temperature on this reaction over a range of 50–160 °C, and we obtained the maximum ^{19}F FDF yield at 80–100 °C (Figure 2b). We confirmed the incorporation of ^{19}F -fluorine by fluorine nuclear magnetic resonance (NMR) (Figure 2c) and high-resolution mass spectrometry (HRMS) analysis (Figure 2d).

Radiochemistry. We treated tetrabutylammonium bicarbonate with $^{18}\text{F}^-$ to generate tetrabutylammonium ^{18}F -fluoride, which was then reacted with compound 7 in DMSO in the presence of *m*-CPBA. The reaction was stirred at 80 °C for 30 min (Figure 2a,g). This scheme afforded an overall 7.4%

decay-corrected radiochemical yield of ^{18}F FDF [$n = 14$ batches, average production 88.4 mCi/batch (3.27 GBq/batch), and 578.8 Ci/mmol (21 415.6 GBq/mmol) molar activity (specific activity) with 99.9% radiochemical purity, overall synthesis time 51 min]. Figure 2e shows the high-performance liquid chromatography-ultraviolet (HPLC-UV) chromatogram, and Figure 2f shows the HPLC-gamma chromatogram of ^{18}F FDF from a typical radiochemical reaction. Thus, inclusion of the 5,5-dimethyl substituent on the furanone ring was a successful strategy to improve compound stability to the point that it could tolerate the harsh radiosynthetic conditions.

Pharmacokinetics of FDF. The plasma protein binding of FDF was determined in vitro for mouse, dog, and human. Binding was approximately 99% in dog and human plasma, and 97.5% in mouse plasma. Thus, FDF is highly bound to plasma proteins across species with free fractions of about 0.99–2.5% of the total plasma FDF concentration (Figure 1f). The plasma half-life of FDF in CD-1 mice was 1.2 h (Figure 3a). Biodistribution analysis showed a significantly higher uptake of FDF in the kidney (average 8.87 nmol/g tissue) than the liver (overall average 0.61 nmol/g tissue) or other organs (Figure 3b). The very low levels of uptake in the lung, heart, liver, brain, and muscle suggest that FDF exhibits very low affinity for these organs, and high kidney uptake may be attributable to renal clearance. Also, we analyzed the tissues to evaluate the potential of FDF for defluorination in vivo. The defluorinated metabolite was reliably detected in kidneys (0.01 nmol/g

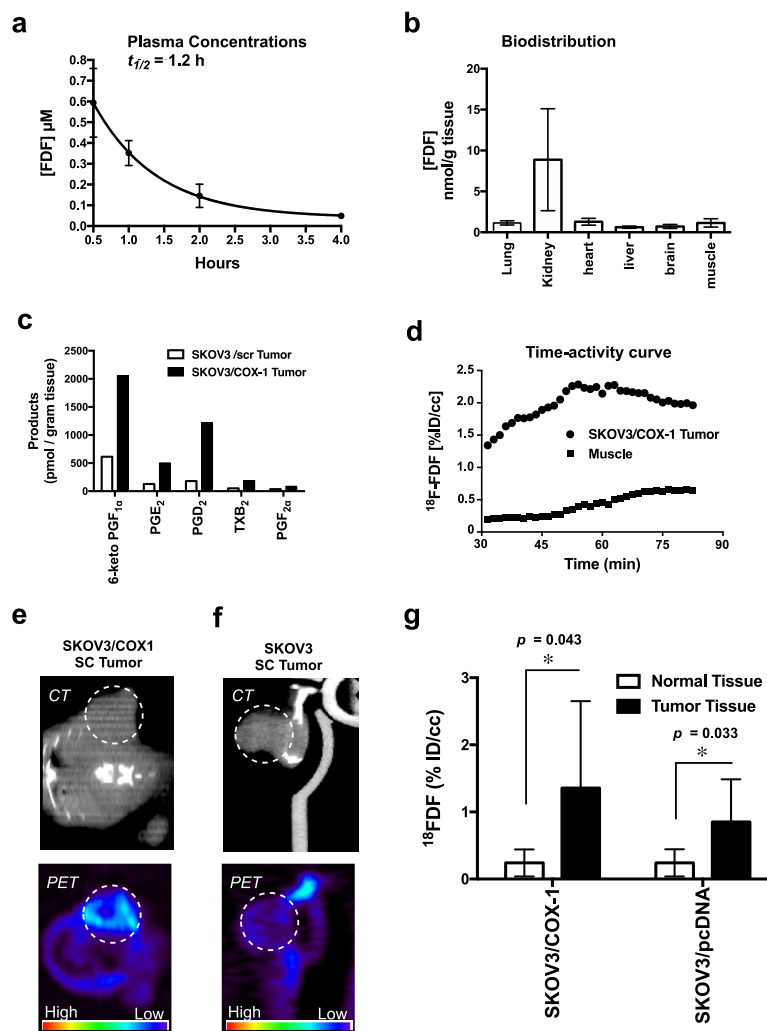


Figure 3. (a) In vivo plasma half-life of FDF in CD-1 mice. (b) In vivo biodistribution in C57BL/6 mice. (c) Level of COX-1 products in SKOV3/pcDNA tumors and SKOV3/COX-1 tumors analyzed by LC–MS/MS (d) time–activity curve of [^{18}F]FDF in subcutaneous tumor vs muscle tissues. (e) In vivo PET/CT imaging of SKOV3/COX-1 (high COX-1-expressing) subcutaneous tumors implanted in mice. (f) In vivo PET/CT imaging of SKOV3/pcDNA (low COX-1-expressing) subcutaneous tumors implanted in mice. (g) Image analysis of [^{18}F]FDF signal intensity in subcutaneous tumors vs muscle by AMIDE software.

tissue), but levels were below the quantification limit in other organs, suggesting minimal de-fluorination of FDF.

Human Ovarian Cancer Xenograft Model. We have developed a dual human tumor xenograft model that enables evaluation of [^{18}F]FDF radiotracer uptake by a high COX-1-expressing and a low COX-1-expressing tumor simultaneously in a single animal. We have optimized reproducibility in this model by using the SKOV3 ovarian cancer cell line transfected with the empty vector (SKOV3/pcDNA), which naturally expresses quite low levels of COX-1, and SKOV3 cells transfected with the COX-1 gene (SKOV3/COX-1), which express high levels of COX-1. The transfection of the COX-1 gene into the parental SKOV3 cell line results in stable protein expression levels similar to those in the naturally expressing OVCAR-3 ovarian cancer cell line (Figure 1d). The SKOV3/COX-1 and SKOV3/pcDNA cells were chosen over the OVCAR3 line because tumor xenografts from OVCAR3 cells grow extremely slowly.

To confirm the differential expression of COX-1 in vivo, we determined the level of PGs and TXs in tumor xenografts

derived from SKOV3/pcDNA and SKOV3/COX-1 cells. Concentrations of PGs and TX in SKOV3/COX-1 tumors were nearly fourfold greater than those in SKOV3/pcDNA tumors (Figure 3c). It is noteworthy that SKOV3/pcDNA and SKOV3/COX-1 cells do not express COX-2.

In Vivo PET/CT Imaging of COX-1 in Ovarian Tumors.

We evaluated [^{18}F]FDF as a COX-1-targeted PET imaging agent in two preclinical mouse models of ovarian cancer. The first included the use of subcutaneous human cell line xenograft tumors to validate target specificity of [^{18}F]FDF. The second strategy utilized an intraperitoneal (i.p.) mouse model of ovarian cancer that is more physiologically relevant to human ovarian cancer.

In the first set of experiments, subcutaneous xenograft tumors derived from SKOV3/COX-1 and SKOV3/pcDNA cells were established on the left and right hind flanks, respectively, of female athymic nude mice. The tumor xenografts were allowed to grow to approximately 750–1000 mm³. To determine the time-point at which maximal tumor uptake occurs, we performed a 1.5 h dynamic PET scan

initiated with [^{18}F]FDF i.p. injection. The resulting time–activity curve showed a maximal tumor uptake of [^{18}F]FDF at around 1 h post injection with a fourfold increased uptake by the tumor compared to muscle tissues (Figure 3d). For in vivo PET/CT imaging of tumors, we administered [^{18}F]FDF to tumor-bearing mice at a dose range of 400–700 μCi (0.0148–0.0259 GBq) per mouse (i.p. injection). Following 1 h, the animals were placed in a micro-PET/CT Focus 220 for imaging. The results demonstrated that [^{18}F]FDF accumulated in the high COX-1-expressing SKOV3/COX-1 xenografts to greater levels (Figures 3e and S30) than in the low COX-1-expressing SKOV3/pcDNA xenografts (Figure 3f). The PET images were analyzed using AMIDE software and corrected for injected dose and body weight. Three-dimensional regions of interest (ROI) were drawn around the tumors and surrounding normal tissues separately. Figure 3g shows the quantitative representation of uptake of [^{18}F]FDF into the SKOV3/COX-1 and SKOV3/pcDNA tumors as compared to [^{18}F]FDF uptake in the leg muscle. Over the group of animals imaged, tracer accumulation in the high COX-1-expressing tumor xenograft ROI (mean \pm sd = 1.4 ± 1.3 , $p = 0.043$, $n = 5$) was three- to sixfold greater than that in the muscle ROI (mean \pm sd = 0.24 ± 0.2 , $n = 5$), and tracer accumulation in the low COX-1-expressing tumor xenograft ROI (mean \pm sd = 0.84 ± 0.64 , $p = 0.033$, $n = 5$) was two- to threefold greater than that in the muscle ROI (mean \pm sd = 0.24 ± 0.20 , $n = 5$), consistent with the differential levels of COX-1 expression.

To evaluate the ability of [^{18}F]FDF to target ovarian cancer under more physiologically relevant conditions, we used a SKOV3/COX-1 peritoneal tumor model. In this model, SKOV3/COX-1 cells [1×10^7 in 200 μL sterile phosphate buffered saline (PBS)] were injected intraperitoneally into 6-week-old female nude mice, and the tumors were allowed to grow for a period of up to 3 months. Imaging commenced at the first sign of ascites. Dynamic scanning over 0–9 min revealed that the time-point of maximal [^{18}F]FDF uptake in the peritoneal tumors was ~ 5 min (Figure 4a). For in vivo tumor imaging, the animals were dosed with 500–650 μCi (0.0185–0.0241 GBq) [^{18}F]FDF (50 μL , retro-orbitally) and imaged in the Inveon micro-PET/CT (Siemens) at 5 min postinjection of the radiotracer. As a contrast agent for CT, ioversol injection Optiray 320 was dosed (200 μL , intraperitoneally) 10 min prior to [^{18}F]FDF. In this model, tumors form throughout the peritoneal cavity with varying sizes and shapes, making their identification by PET/CT much more challenging than in the subcutaneous xenograft model. However, we were able to correctly visualize multiple peritoneal tumors in each animal by [^{18}F]FDF/PET (Figures 4b,c and S31). The normalized tumor uptake (mean \pm sd = 25 ± 6 , $p < 0.0004$, $n = 6$) was approximately fivefold higher than the uptake in normal muscle tissues (Figure 4d, mean \pm sd = 3.4 ± 0.9 , $n = 6$). These results demonstrate that signals from [^{18}F]FDF can distinguish a COX-1-expressing tumor in the low background of COX-1 expression in the peritoneal cavity, a key requirement for its use in the imaging of ovarian cancer in clinical settings.

DISCUSSION

The diarylheterocyclic scaffolds yielded the highest number of potent and selective COX-2 inhibitors, such as celecoxib, rofecoxib, and valdecoxib (Figure 1a).²⁷ The key determinant of the COX-2 selectivity of these compounds is the presence on one of the aromatic rings of a sulfonamide or a

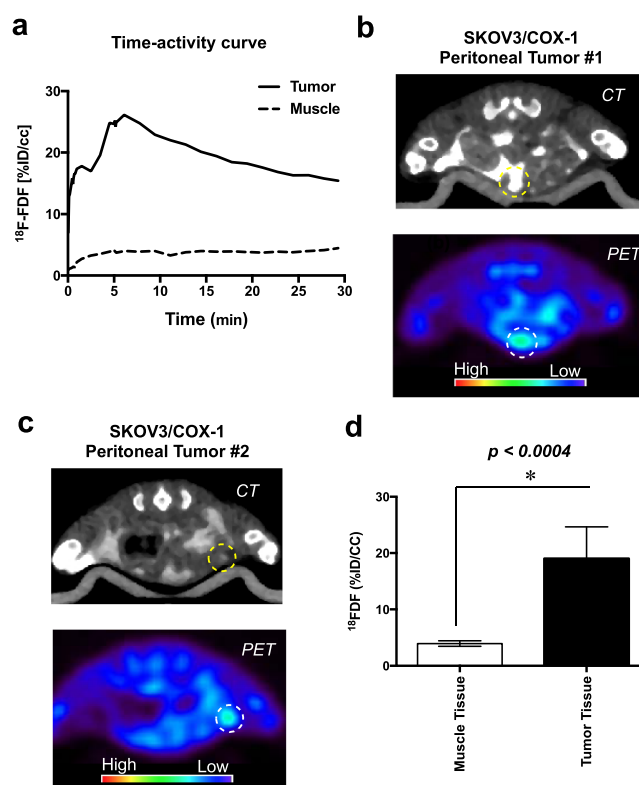


Figure 4. (a) Time–activity curve of [^{18}F]FDF in peritoneal tumor vs muscle. (b) In vivo PET/CT imaging of SKOV3/COX-1 peritoneal tumor #1. (c) In vivo PET/CT imaging of SKOV3/COX-1 peritoneal tumor #2. (d) Image analysis of [^{18}F]FDF signal intensity in peritoneal tumors vs muscle.

methylsulfone that inserts into a side-pocket in the cyclooxygenase active site that is only accessible in COX-2.^{28,29} Thus, the COX-1-selective inhibitor SC-560, a diarylpyrazole analog, was discovered via the deletion of the sulfonamide group from celecoxib.³⁰ SC-560 has been extensively used as an in vivo probe for COX-1's involvement in biological responses;^{31,32} however, when [^{11}C]SC-560 was synthesized for PET imaging, COX-1-dependent accumulation in tissues could not be demonstrated.³³ This failure is likely because SC-560 has not been optimized for in vivo activity and suffers from multiple liabilities, including poor solubility and pyrazole-associated off-target effects.^{34,35} The diarylfuranone scaffold that yielded rofecoxib appears more promising as a starting point for the synthesis of a COX-1-selective inhibitor. Rofecoxib's aqueous solubility is higher, and it has been associated with fewer off-target effects than celecoxib.³⁵ In general, the clog P_s of simple diarylfuranones (1.8–3.0) promise a reasonably higher level of water solubility than those of many typical drug-like scaffolds that have been used for the synthesis of COX-2 inhibitors.

The key functional group for the COX-2-selectivity of rofecoxib is the sulfonylmethyl group on the C-4 aromatic ring.²⁹ Consistently, we previously demonstrated that removal of this group reverses the selectivity of the molecule from COX-2 to COX-1. Although the resulting 3,4-diphenylfuranone is a weak COX-1-selective inhibitor ($\text{IC}_{50} = 5.9 \mu\text{M}$)³⁶ it served as a promising scaffold for optimization by functionalization, leading to the discovery of VU0487836 (Figure 1a).³⁶ To enable its use as a PET imaging agent, VU0487836 was constructed with a metabolically stable fluorine atom that

could be readily incorporated as ^{18}F radioactive fluorine at a late stage in synthesis. However, after multiple attempts to incorporate ^{18}F into this molecule failed, we hypothesized that VU0487836's γ -lactone ring is unstable under the highly basic ($\text{pH} \approx 11$) radiomimetic conditions. Thus, as described here, we developed the synthetic procedures and performed the additional structure–activity optimization required to obtain COX-1-selective inhibitors that include a furanone ring-stabilizing 5,5-dimethyl substituent. This effort led to the discovery of FDF.

Despite the addition of the 5,5-dimethyl group, we found that commonly used techniques^{37–39} were extremely limited for the nucleophilic aromatic deiodofluorination reaction required to synthesize ^{18}F FDF. We hypothesize that the failure of these nucleophilic aromatic substitutions is due to the presence of the strongly electron-withdrawing furanone nucleus that induces nucleophilic fluorination of the hypervalent iodine. To stabilize the newly created inner-halogen bond, it is possible that a lone pair of electrons of the hypervalent iodine delocalizes to create a quinone-like inner-halogen intermediate that is incapable of conversion into ^{18}F FDF. To address this problem, we first treated the iodonium salt with TBAF in the presence of *m*-CPBA as a catalyst. Interestingly, this reaction afforded the desired ^{19}F -product (36% yield). To investigate whether this is an oxidation phenomenon, we replaced *m*-CPBA with oxone or potassium peroxodisulfate. No ^{19}F FDF was identified in the reaction mixture, suggesting that *m*-CPBA was not acting as an oxidizing agent in this reaction. To uncover *m*-CPBA's mechanism of action, we utilized a Lewis acid, *m*-chlorobenzoic acid (*m*-CBA), in its place. This reaction afforded ^{19}F FDF in 33% yield, suggesting that *m*-CPBA reacts in situ with solvent DMSO to form *m*-CBA, which then catalyzed the reaction to form the ^{19}F FDF product. Later, we replaced *m*-CBA with HCl and found that it also successfully produced ^{19}F FDF ($\sim 30\%$ yield). The strong electrophilic nature of iodine is the basis for the hypervalent iodine chemistry that creates a position in the molecule that is susceptible to nucleophilic attack. Thus, iodonium salts have been designated a hyperleaving group. We propose that the Lewis acid inhibits the delocalization of the lone pair of electrons of the hypervalent iodine. This favors the formation of the transition state (Figure 2g) of the reductive elimination that is key to the reaction of hypervalent iodine, thereby forming the ^{18}F FDF product. It is likely that electron-trapping by the Lewis acid disfavors the formation of the inactive quinone-like intermediate that inhibits the reductive elimination of hypervalent iodine.

Our experiments demonstrate the successful development of a furanone-based COX-1-targeted in vivo PET/CT imaging probe for ovarian cancer. ^{18}F -FDF displays targeted uptake in two distinct animal models of ovarian cancer, demonstrating the selectivity for ovarian cancer xenografts expressing high levels of COX-1 compared to those that express low levels of COX-1 or surrounding tissue. It should be noted that the uptake into subcutaneous ovarian tumors was slower than into peritoneal tumors as demonstrated by quantitative analysis of tumor biodistribution of ^{18}F -FDF in vivo. This difference might be because the subcutaneous tumors are less vascularized than the peritoneal tumors, which are physiologically more relevant to human ovarian cancer.

To achieve this success, we developed a simple one-pot procedure for the chemical synthesis of fluorine-containing

furanone derivatives and evaluated them as COX-1-targeted PET/CT imaging agents. Although a vast majority of these compounds were selective against both purified COX-1 protein and COX-1 activity in intact cancer cells, only FDF exhibited adequate stability during radio ^{18}F fluorination, reasonably long in vivo plasma half-life, sufficient metabolic stability in the circulation, and acceptable plasma protein binding characteristics. ^{18}F FDF showed efficient COX-1-dependent uptake and enrichment to result in a detectable level of concentration in tumor tissues. These experiments confirm ^{18}F FDF's utility in COX-1-targeted in vivo PET/CT imaging of xenograft tumors of ovarian cancer in rodents. These in vivo results suggest that the binding of ^{18}F FDF with COX-1 is the major determinant of its tumor uptake and support the conclusion that ^{18}F FDF-PET is a feasible imaging approach for visualization of ovarian tumors expressing elevated levels of COX-1 in preclinical and clinical settings.

CONCLUSIONS

We report the discovery of FDF, a furanone-based COX-1-targeted agent. Selective COX-1 binding of FDF and inhibition were confirmed in assays using purified enzyme and in ovarian cancer cells expressing elevated levels of COX-1. FDF does not bind with COX-2 in any of these settings. FDF exhibits adequate metabolic stability, protein binding, and plasma half-life to enable its use for in vivo imaging. As the radiosyntheses of furanone-based radiopharmaceuticals are extremely rare, we developed an iodonium-based method for radiolabeling of FDF involving a novel Lewis acid-catalyzed nucleophilic aromatic deiodo ^{18}F fluorination reaction. We report the application of ^{18}F FDF in the detection of COX-1 in mouse models of ovarian cancer, including both subcutaneous and i.p. human tumor xenografts. In vivo uptake of ^{18}F FDF was selective for COX-1 overexpressing tumors over normal tissues. ^{18}F FDF represents the first feasible radiotracer validated for targeted PET/CT imaging of neoplastic tissues expressing elevated levels of the COX-1 isozyme.

EXPERIMENTAL SECTION

Synthesis of Compounds. We purchased compounds a–c from Sigma-Aldrich, synthesized d–g using literature methods,^{40–42} and developed synthetic methods for 1–7. Spectra and chromatograms of all new compounds are listed in the Supporting Information.

Solvents and Reagents. ACS grade reagents and anhydrous solvents were purchased from Sigma-Aldrich, Fisher, or VWR Chemical Companies, and used without further purification.

Chromatography. Plastic-backed microplates were used for analytical silica gel thin-layer chromatography (TLC) of crude reaction mixtures. An ultraviolet illuminator at 254–365 nm wavelength was used for spot visualization. Flash or gravity column chromatography was performed using standard grade silica gel from Sorbent Technologies.

HPLC Conditions. Waters HPLC system with a photometric diode array detector (at 254 nm wavelength) was used for determination of purity of the final compounds. The instrument was equipped with a Supelco Supelcosil C-18 reverse-phase column (15 cm \AA –3 mm, 5 μm) using the following chromatographic conditions: component A— H_2O with 5 mM octanesulfonic acid ($\text{pH} \approx 3$) and component B—acetonitrile with 10% component A gradient: 40% B to 90% B

in 9.5 min followed by 5.5 min hold at 90% B, flow: 1.0 mL/min, column: Supelco C18 25 × 0.46 cm, 5 μm, held at 40 °C.

Nuclear Magnetic Resonance. A Bruker AV-I console operating at 600 MHz was used for ¹H NMR and ¹H correlation spectroscopy experiments of all new compounds. A 9.4 T Oxford magnet was equipped with the Bruker AV-I instrument in which the following experimental conditions were applied: data matrix—2048 × 512, sweep width—13 ppm, recycle delay—1.5 s, and scans per increment—4. We processed the acquired data using a squared sine-bell window function, which were symmetrized, and displayed in magnitude mode. A Bruker DRX console operating at 150 MHz, equipped with an 11.7 T Oxford magnet, was used for ¹³C, heteronuclear single quantum coherence, and heteronuclear multiple bond correlation NMR experiments.

High-Resolution Mass Spectrometry. A quantum triple quadrupole instrument equipped with a Thermo-Electron Surveyor pump is used for HRMS analysis of synthesized compounds in positive or negative ion mode.

Melting Point. Melting points were determined using Gallenkamp 7936G capillary melting point apparatus and were uncorrected.

Synthesis of Furanone Compounds 1–6. Anhydrous dichloromethane (50 mL) was added to a mixture of substituted hydroxy ketone (5 mmol), substituted-phenylacetic acid (5.2 mmol), *N*-cyclohexyl-*N'*-(2-morpholinoethyl)-carbodiimide methyl-*p*-toluenesulfonate (CMC, 5.2 mmol), and *N,N*-dimethylaminopyridine (2.6 mmol). After stirring for 18 h at 25 °C DBU (7.8 mmol) was added to the reaction mixture, which was then refluxed (40–45 °C) for 3 h. The reaction mixture was cooled to room temperature, water (40 mL) was added to quench the reaction, and the mixture was then extracted with dichloromethane (3 × 100 mL). The combined organic layers were dried over Na₂SO₄ and concentrated in vacuo. The product was purified by crystallization or by silica gel column chromatography using *n*-hexane/ethyl acetate (4:1), or by HPLC with a photodiode-array detector using a C-18 column. This method gave compounds 1–6 (70–75% yield) at 99.5–99.9% HPLC purity.

5,5-Dimethyl-3,4-diphenylfuran-2(5H)-one, 1. The title compound, which was synthesized using the general method described above, was obtained as a white solid, 0.99 g, 75% yield, melting point 159–160 °C. ¹H NMR (600 MHz, DMSO-*d*₆): δ 1.54 (s, 6H), 7.26–7.45 (m, 10H). ¹³C NMR (150.9 MHz, DMSO-*d*₆): 24.76, 85.61, 125.44, 127.81, 128.01, 128.17, 128.29, 128.82, 128.93, 129.06, 129.31, 129.77, 131.96, 166.54, 170.35. HRMS *m/z*: calcd for [C₁₈H₁₆O₂ + H]⁺, 265.1262; found, 265.1218. HPLC retention time 12.23 min and HPLC purity 99.9%.

5,5-Dimethyl-3-phenyl-4-(*p*-tolyl)furan-2(5H)-one, 2. The title compound, which was synthesized using the general method described above, was obtained as a white solid, 0.97 g, 70% yield, melting point 191–192 °C. ¹H NMR (600 MHz, DMSO-*d*₆): δ 1.53 (s, 6H), 2.32 (s, 3H), 7.18 (d, *J* = 8.5 Hz, 2H), 7.25 (d, *J* = 8.5 Hz, 2H), 7.27–7.29 (m, 5H). ¹³C NMR (150.9 MHz, DMSO-*d*₆): 20.81, 24.87, 85.63, 125.21, 127.76, 128.04, 128.23, 128.92, 128.96, 129.42, 129.96, 138.66, 166.65, 170.41. HRMS *m/z*: calcd for [C₁₉H₁₈O₂ + H]⁺, 279.1365; found, 279.1376.

HPLC retention time 11.41 min, and HPLC purity 99.9%.

3-(4-Fluorophenyl)-5,5-dimethyl-4-phenylfuran-2(5H)-one, 3. The title compound, which was synthesized using the

general method described above, was obtained as a white solid, 1.02 g, 72% yield, melting point 92–93 °C. ¹H NMR (600 MHz, DMSO-*d*₆): δ 1.70 (s, 6H), 7.25–7.31 (m, 2H), 7.32–7.34 (m, 2H), 7.42–7.44 (m, 1H), 7.92–7.95 (m, 4H). ¹³C NMR (150.9 MHz, DMSO-*d*₆): 24.93, 84.39, 115.89, 116.03, 125.81, 125.83, 128.17, 128.53, 132.24, 132.31, 133.75, 164.07, 164.47, 166.14, 198.09. HRMS *m/z*: calcd for [C₁₈H₁₅FO₂-F + Na]⁺, 287.1073; found, 287.1074. HPLC retention time 12.97 min, HPLC purity 99.9%.

3-(4-Fluorophenyl)-5,5-dimethyl-4-(*p*-tolyl)furan-2(5H)-one, 4. The title compound, which was synthesized using the general method described above, was obtained as a white solid, 1.09 g, 74% yield, melting point 163–164 °C. ¹H NMR (600 MHz, DMSO-*d*₆): δ 1.52 (s, 6H), 2.32 (s, 3H), 7.13 (d, *J* = 8.5 Hz, 2H), 7.19 (d, *J* = 8.5 Hz, 2H), 7.25–7.26 (m, 2H), 7.33–7.36 (m, 2H). ¹³C NMR (150.9 MHz, DMSO-*d*₆): 20.81, 24.78, 85.72, 115.03, 115.17, 124.25, 126.34, 126.36, 127.71, 128.80, 129.51, 131.09, 131.15, 138.75, 160.96, 162.59, 166.58, 170.36. HRMS *m/z*: calcd for [C₁₉H₁₇FO₂ + H]⁺, 297.1213; found, 297.1282. HPLC retention time 12.95 min, HPLC purity 99.9%.

3-(3-Fluorophenyl)-5,5-dimethyl-4-(*p*-tolyl)furan-2(5H)-one, 5. The title compound, which was synthesized using the general method described above, was obtained as a white solid, 1.05 g, 71% yield, melting point 158–159 °C. ¹H NMR (600 MHz, DMSO-*d*₆): δ 1.53 (s, 6H), 2.33 (s, 3H), 7.10–7.14 (m, 3H), 7.19 (d, *J* = 8.5 Hz, 2H), 7.28 (d, *J* = 8.5 Hz, 2H), 7.30–7.34 (m, 1H). ¹³C NMR (150.9 MHz, DMSO-*d*₆): 20.81, 24.69, 85.83, 115.09, 115.23, 115.54, 115.69, 125.09, 125.11, 127.64, 128.59, 129.51, 130.06, 130.12, 138.90, 160.75, 162.36, 167.67, 170.05. HRMS *m/z*: calcd for [C₁₉H₁₇FO₂ + H]⁺, 297.1213; found, 297.1275. HPLC retention time 12.96 min, HPLC purity 99.9%.

3-(4-Iodophenyl)-5,5-dimethyl-4-(*p*-tolyl)furan-2(5H)-one, 6. The title compound, which was synthesized using the general method described above, was obtained as a yellow solid, 1.48 g, 73% yield, melting point 197–198 °C. ¹H NMR (600 MHz, DMSO-*d*₆): δ 1.52 (s, 6H), 2.33 (s, 3H), 7.08 (d, *J* = 8.5 Hz, 2H), 7.17 (d, *J* = 8.5 Hz, 2H), 7.25 (d, *J* = 8.7 Hz, 2H), 7.67 (d, *J* = 8.7 Hz, 2H). ¹³C NMR (150.9 MHz, DMSO-*d*₆): 20.84, 24.77, 85.89, 95.08, 124.47, 127.68, 128.69, 129.54, 131.00, 136.95, 138.87, 167.15, 170.10. HRMS *m/z*: calcd for [C₁₉H₁₇IO₂ + Na]⁺; found, 427.0165. HPLC retention time 12.23 min, HPLC purity 99.9%.

(4-(5,5-Dimethyl-2-oxo-4-(*p*-tolyl)-2,5-dihydrofuran-3-yl)-phenyl)(4-methoxyphenyl)iodonium Tosylate, 7. A solution of 2,2,2-trifluoroethanol (2.5 mL) in anhydrous dichloromethane (2.5 mL) was added to a mixture of compound 6 (0.5 g, 1.2 mmol), 3-chloroperbenzoic acid (0.26 g, 1.2 mmol), and anisole (0.135 g, 1.2 mmol), followed by 4-toluenesulfonic acid (0.24 g, 1.2 mmol). After stirring for 4 h at 25 °C, the solvent was evaporated in vacuo, and the resultant residue was chromatographed on silica gel. The column was first washed with *n*-hexane/EtOAc (4:1) to remove impurities, and the product was then eluted with CHCl₃/MeOH/NH₄OH (35:7:1). The solvent was evaporated in vacuo to dryness. EtOAc (2 mL) was added to the residue and mixed vigorously to afford the product in pure form as a white solid, 0.57 g, 70% yield, melting point 238–240 °C. ¹H NMR (600 MHz, DMSO-*d*₆): δ 1.52 (s, 6H), 2.28 (s, 3H), 2.32 (s, 3H), 3.79 (s, 3H), 7.04 (d, *J* = 8.5 Hz, 2H), 7.11 (d, *J* = 8.6 Hz, 2H), 7.16 (d, *J* = 8.5 Hz, 2H), 7.24 (d, *J* = 8.6 Hz, 2H), 7.37 (d, *J* = 8.6 Hz, 2H), 7.47 (d, *J* = 8.5 Hz, 2H), 8.10 (d, *J* = 8.6 Hz, 2H),

8.12 (d, $J = 8.6$ Hz, 2H). ^{13}C NMR (150.9 MHz, DMSO- d_6): 20.75, 20.82, 24.61, 55.65, 86.17, 105.88, 117.00, 117.38, 124.09, 125.47, 127.65, 127.99, 128.30, 129.53, 131.80, 133.42, 134.50, 137.18, 137.49, 139.05, 145.82, 161.87, 168.56, 169.90. HRMS m/z : calcd for 511.0847 [$\text{C}_{26}\text{H}_{24}\text{IO}_3 - \text{OTs}]^+$; found, 511.0759. HPLC retention time 9.53 min, HPLC purity 99.5%.

Radiosynthesis of [^{18}F]FDF, [^{18}F]4. In a typical reaction, a mixture $^{18}\text{F}^-$ fluoride 1194.6 mCi (44.2 GBq) in water (1 mL) and acetonitrile (2 mL) was added to a stirred aqueous tetrabutylammonium bicarbonate (0.038 M, 1 mL) solution. The solvent was evaporated using a stream of argon (6–10 psi, 15–25 mL/min) at 91 °C and complete dryness was achieved by repetitive evaporation with acetonitrile ($3 \times 200 \mu\text{L}$). The dried [^{18}F]-TBAF was dissolved in anhydrous DMSO (0.5 mL) and was added to a solution of iodonium precursor (7, 4 mg, 0.0065 mmol) and *m*-CPBA (1.3 mg, 0.0075 mmol) in DMSO (0.5 mL). The reaction mixture was stirred at 80 °C for 30 min. A radio-HPLC was used for the purification of [^{18}F]-FDF [C18, 250 \times 10, 8 μm , EtOH/water (50:50), flow rate 5 mL/min, R_f 13.12 min]. The [^{18}F]-FDF peak was collected, evaporated, and the radiotracer was formulated using EtOH/saline, 1:9 v/v, 112 mCi (4.14 GBq), decay-corrected radiochemical yield 9.3%, radiochemical purity 99.9%, overall synthesis time 51 min).

Inhibition of Purified Cyclooxygenase Isozymes. We evaluated the COX-1 and COX-2 inhibitory activities of test compounds 1–7 using a previously described radio-TLC assay.²⁴

Western Blot Analysis. Cell lines were grown in 100 mm plates (Sarstedt) to 50% confluence and were harvested by scraping into PBS. The cells were centrifuged at 4 °C, 200g for 5 min. The pellets were resuspended in 200 μL of M-PER (Pierce) and frozen at –80 °C. Cell lysates (20 μg) or COX-1/-2 (5 ng, positive control) were loaded onto a 4–20% 10-well, 50 μL , Mini-PROTEAN TGX gel (Bio-Rad). Following electrophoresis and transfer, the blot was incubated overnight with a murine monoclonal antibody raised against human COX-1 or COX-2 (Santa Cruz) at 1:200 dilution. The presence of the antibody was detected by treatment with IRDye 680LT donkey antimouse IgG (1:10 000, LI-COR).

Inhibition of Cyclooxygenases in Cells. We evaluated the ability of test compounds 1–7 to inhibit COX-1 and COX-2 in intact cells using a published procedure.²⁴ Briefly, both OVACR3 cells and 1483 HNSCC cell lines were plated in 6-well plates (Sarstedt) and grown to 60% confluence. Serum-free medium (2 mL) was added per well with 0, 0.04, 0.2, 0.5, 1.0, and 5.0 μM final concentration of FDF for 30 min at 37 °C. The final concentration of DMSO was 0.5% in all wells. The medium (1 mL) was removed, and [$1\text{-}^{14}\text{C}$]-arachidonic acid (57 mCi/mmol, 2.11 GBq/mmol, NEC661, PerkinElmer) was added to provide a 4 μM final concentration. At the end of the 30 min, 37 °C incubation, an aliquot of the medium (0.4 mL) was removed from each well and added to a 0.6 mL ice-cold termination solution (Et₂O/CH₃OH, 1 mol/L citrate 30:4:1, pH 4). The organic layer was spotted on 20 \times 20 TLC plates, developed, and quantitated on the Bioscan AR-2000 for the remaining arachidonic acid substrate compared to the vehicle-only cells.

Plasma Protein Binding. We evaluated the binding characteristics of FDF to plasma proteins in vitro to identify its unbound free fractions. We determined the percent of FDF bound to protein using a fast gradient elution liquid chromatography–mass spectrometry (LC–MS)/MS at 0 and

4.5 h of incubation of the compound with the plasma from mouse, human, and dog at 37 °C. The assay was performed using a high-throughput dialysis micro-equilibrium device. The unbound fraction was calculated by dividing the concentration of the buffer side by the concentration of the protein side.⁴³ Percent recovery was calculated by dividing the sum of the buffer and protein chambers by the time of 0 concentration after 4.5 h.

Radiomimetic Chemistry. A solution of tetrabutylammonium ^{19}F -fluoride (11 mg, 0.035 mmol) in anhydrous DMSO (0.5 mL) was added to a solution of the iodonium precursor 7 (6 mg, 0.0084 mmol) and *m*-CPBA (1.6 mg, 0.0084 mmol) in DMSO (0.5 mL). The reaction mixture was stirred for 30 min at 80 °C. After cooling to room temperature, the reaction mixture was poured into a silica column and eluted with *n*-hexane/ethylacetate (4:1) to afford the fluorinated product [^{19}F]FDF (compound 4, 3.4 mg, 33% isolated yield, 99.9% HPLC purity, $n = 12$).

LC–MS/MS Analyses. All LC–MS/MS analyses were carried out on a Shimadzu LC system in-line with a SCIEX 3200 QTrap mass spectrometer. The 3200 QTrap was equipped with an electrospray source and operated in positive ion mode.

Mice. We performed all ex vivo and in vivo animal experiments and ethical conducts according to the methods approved by the Vanderbilt University Institutional Animal Care and Use Committee (IACUC) and the National Institute of Health (NIH) guidelines.

Plasma Concentrations. C57BL/6 mice (male, 25 g, Charles River Labs) were dosed with FDF (10 mg/kg, i.p.). Following 0.5, 1, 2, or 4 h the mice (three per time point) were euthanized by lethal anesthesia, and blood was collected by cardiac puncture. Blood was drawn into heparinized 1 mL syringes with 22 g, 1 in needles, and gently expelled into 1.5 mL tubes containing 10 μL of heparin (on ice). After mixing, the tubes were centrifuged at 2300g for 5 min at 4 °C. The upper plasma layer was transferred into fresh tubes for storage at –80 °C until processing.

FDF was extracted from plasma by liquid–liquid extraction, and an internal standard (compound 5) was added to the samples. Then, the samples were diluted with an equivalent of water containing 1% acetic acid. After a 2 \times volume of ethyl acetate was added, the samples were mixed well and centrifuged briefly to promote phase separation. The upper ethyl acetate layer was removed to clean the vessels and dried under nitrogen. Dried samples were reconstituted in 1:1 water/methanol and analyzed via LC–MS/MS. The analyte was chromatographed on a Phenomenex Lux Amylose column (25 \times 0.46 cm). The mobile phase was 1:1 water/acetonitrile (each with 0.1% formic acid), and the flow rate was 1.0 mL/min. Mass spectrometric detection of the analyte and internal standard (compound 5) was accomplished via selected reaction monitoring (SRM). The SRM transition for both was m/z 279 \rightarrow 221, and the samples were quantitated against a standard curve prepared in mouse plasma, which was processed and analyzed alongside the unknown samples.

Biodistribution. To evaluate the biodistribution and potential for defluorination, we analyzed the major organs of C57BL/6 mice injected with unlabeled FDF. C57BL/6 mice (male, 30 g, Charles River Labs, three per group) were dosed with FDF (10 mg/kg, i.p.) at 10 min intervals. Following 60 min, the mice were sacrificed by anesthesia overdose followed by immediate removal of brain, lungs, heart, kidney, liver, and

muscle. Tissues were rinsed in cold PBS and blotted, then placed into pre-labeled foil squares between blocks of dry ice. Organs and tissues were stored at $-80\text{ }^{\circ}\text{C}$ until LC/MS–MS analysis.

For analysis, tissues were weighed and then placed in 3 mL of acetonitrile in a Tenbroeck tissue grinder. The tissues were pulverized via sonication and mechanical grinding. The homogenate was removed to a clean vessel, and the Tenbroeck tissue grinder was rinsed with 1 mL of acetonitrile, which was added to the homogenate. The homogenate was stored overnight at $-20\text{ }^{\circ}\text{C}$ and then centrifuged at $2060g$ at $4\text{ }^{\circ}\text{C}$ for 10 min. The clear supernatant was removed to a clean test tube and dried under nitrogen. The dried sample was reconstituted in $60\text{ }\mu\text{L}$ of methanol followed by $60\text{ }\mu\text{L}$ of water. The reconstituted samples were re-centrifuged to pellet out particulate matter and then analyzed via LC–MS/MS.

The samples were chromatographed on a Phenomenex C18 column ($5 \times 0.2\text{ cm}$). The mobile phase components were water (A) and 1:1 methanol/acetonitrile (B), each containing 0.1% formic acid. A gradient elution scheme was employed in which % B increased from 50 to 100% over 3 min, and the flow rate was 0.32 mL/min . Analyte detection was accomplished via SRM. The SRM transition $m/z\ 279 \rightarrow 236$ was used for quantitation in conjunction with a standard curve of samples prepared in 1:1 methanol/water and interspersed with the tissue samples.

Subcutaneous Tumor Model. Subcutaneous xenograft tumors derived from high COX-1-expressing human SKOV3/COX-1 cells and low COX-1-expressing SKOV3/pcDNA cells (1×10^4 in $100\text{ }\mu\text{L}$ sterile PBS) were established on the left and right hind flanks, respectively, of female athymic nude mice. The tumor xenografts were allowed to grow to approximately $750\text{--}1000\text{ mm}^3$ to ensure that a vascular bed was established within the tumor.

Intraperitoneal Tumor Model. Intraperitoneal xenograft tumors were derived from COX-1-expressing SKOV3/COX-1 cells (1×10^7 in $200\text{ }\mu\text{L}$ sterile PBS) injected intraperitoneally into 6-week-old female nude mice and allowed to grow for a period of up to 3 months.

Tumor Analysis. Tumor tissue was removed from $-80\text{ }^{\circ}\text{C}$ storage and weighed. Then, the tissue was transferred to a Tenbroeck tissue grinder along with deuterated internal standards of the five prostanoids of interest. The tissue was homogenized in 1:1 methanol/PBS, and the homogenate was stored at $-20\text{ }^{\circ}\text{C}$ overnight. The homogenate was centrifuged at $1430g$ for 10 min at $4\text{ }^{\circ}\text{C}$ and $\sim 75\%$ of the clear supernatant was partially dried under nitrogen to reduce the volume and remove methanol. To the partially dried sample, a volume of 1% acetic acid (roughly $5\times$ the amount of homogenate remaining) was added, and the sample was loaded onto a conditioned Phenomenex C18 solid phase extraction cartridge (200 mg). After loading, the cartridge was rinsed with 4 mL of 1% acetic acid, then with 4 mL of 1% acetic acid containing 14% methanol. Finally, the prostanoids were eluted with 3 mL methanol. The eluent was dried under nitrogen and reconstituted in $70\text{ }\mu\text{L}$ of methanol followed by $70\text{ }\mu\text{L}$ of water. The reconstituted samples were analyzed via LC–MS/MS as previously described.

Statistical Analysis. The experimental treatment groups were compared using Student's *t*-test at a statistical significance level of <0.05 . When comparing two data replicates the GraphPad Prism and Microsoft Excel were used for analyses to

obtain data as mean \pm standard deviation of the indicated sample size (*n*) unless stated otherwise.

■ ASSOCIATED CONTENT

📄 Supporting Information

The Supporting Information is available free of charge on the ACS Publications website at DOI: [10.1021/acsomega.9b01093](https://doi.org/10.1021/acsomega.9b01093).

Compound's spectroscopic characterization, chromatographic evaluation, full-length western blot data, and axial, coronal, and sagittal projections of PET/CT images (PDF)

■ AUTHOR INFORMATION

Corresponding Authors

*E-mail: jashim.uddin@vanderbilt.edu. Phone: 615-484-8674. Fax: 615.343-0704 (M.J.U.).

*E-mail: larry.marnett@vanderbilt.edu (L.J.M.).

ORCID

Md. Jashim Uddin: 0000-0003-0020-4866

Md. Imam Uddin: 0000-0001-5611-9666

H. Charles Manning: 0000-0002-5057-4518

Lawrence J. Marnett: 0000-0002-7834-6285

Notes

The authors declare no competing financial interest.

■ ACKNOWLEDGMENTS

This work was supported by research grants from the National Institutes of Health CA128323-4, -5 (M.J.U.), CA182850-01A1 (M.J.U.), CA136465 (L.J.M.), CA89450 (L.J.M.), and Kay Yow Cancer Fund/V Foundation (D.K. and L.J.M.). We are grateful to the Small Molecule NMR Core and the Mass Spectroscopy Research Center for compound characterizations.

■ REFERENCES

- (1) Stewart, S. L.; Harewood, R.; Matz, M.; Rim, S. H.; Sabatino, S. A.; Ward, K. C.; Weir, H. K. Disparities in ovarian cancer survival in the United States (2001-2009): Findings from the CONCORD-2 study. *Cancer* **2017**, *123*, 5138–5159.
- (2) Rauh-Hain, J. A.; Krivak, T. C.; Del Carmen, M. G.; Olawaiye, A. B. Ovarian cancer screening and early detection in the general population. *Rev. Obstet. Gynecol.* **2011**, *4*, 15–21.
- (3) Kurman, R. J.; Visvanathan, K.; Roden, R.; Wu, T. C.; Shih, I.-M. Early detection and treatment of ovarian cancer: shifting from early stage to minimal volume of disease based on a new model of carcinogenesis. *Am. J. Obstet. Gynecol.* **2008**, *198*, 351–356.
- (4) Vidal, F.; Guerby, P.; Luyckx, M.; Haddad, P.; Stoeckle, E.; Morice, P.; Leblanc, E.; Lecuru, F.; Daraï, E.; Classe, J. M.; Pomel, C.; Filleron, T.; Ferron, G.; Querleu, D.; Rafii, A. Are Early Relapses in Advanced-Stage Ovarian Cancer Doomed to a Poor Prognosis? *PLoS One* **2016**, *11*, No. e0147787.
- (5) Das, P. M.; Bast, R. C., Jr. Early detection of ovarian cancer. *Biomarkers Med.* **2008**, *2*, 291–303.
- (6) Robinson, E.; Nandji, M.; Wilkinson, L. L.; Arrowsmith, D. M.; Curtis, A. D. M.; Richardson, A. Preclinical evaluation of statins as a treatment for ovarian cancer. *Gynecol. Oncol.* **2013**, *129*, 417–424.
- (7) Rein, B. J. D.; Gupta, S.; Dada, R.; Safi, J.; Michener, C.; Agarwal, A. Potential markers for detection and monitoring of ovarian cancer. *J. Oncol.* **2011**, *2011*, 475983.
- (8) Rusu, D.; Carlier, T.; Colombie, M.; Goulon, D.; Fleury, V.; Rousseau, N.; Berton-Rigaud, D.; Jaffre, I.; Kraeber-Bodere, F.; Campion, L.; Rousseau, C. Clinical and Survival Impact of FDG PET

in Patients with Suspicion of Recurrent Ovarian Cancer: A 6-Year Follow-Up. *Front. Med.* **2015**, *2*, 46.

(9) Havrilesky, L. J.; Kulusingam, S. L.; Matchar, D. B.; Myers, E. R. FDG-PET for management of cervical and ovarian cancer. *Gynecol. Oncol.* **2005**, *97*, 183–191.

(10) Nanni, C.; Rubello, D.; Farsad, M.; De Iaco, P.; Sansovini, M.; Erba, P.; Rampin, L.; Mariani, G.; Fanti, S. 18F-FDG PET/CT in the evaluation of recurrent ovarian cancer: a prospective study on forty-one patients. *Eur. J. Surg. Oncol.* **2005**, *31*, 792–797.

(11) Ocak, M.; Gillman, A. G.; Bresee, J.; Zhang, L.; Vlad, A. M.; Müller, C.; Schibli, R.; Edwards, W. B.; Anderson, C. J.; Gach, H. M. Folate receptor-targeted multimodality imaging of ovarian cancer in a novel syngeneic mouse model. *Mol. Pharm.* **2015**, *12*, 542–553.

(12) van de Watering, F. C. J.; Rijpkema, M.; Perk, L.; Brinkmann, U.; Oyen, W. J.; Boerman, O. C. Zirconium-89 labeled antibodies: a new tool for molecular imaging in cancer patients. *BioMed Res. Int.* **2014**, *2014*, 203601.

(13) Aljammaz, I.; Al-Otaibi, B.; Al-Hokbany, N.; Amer, S.; Okarvi, S. Development and pre-clinical evaluation of new 68Ga-NOTA-folate conjugates for PET imaging of folate receptor-positive tumors. *Anticancer Res.* **2014**, *34*, 6547–6556.

(14) Sundar, S.; Neal, R. D.; Kehoe, S. Diagnosis of ovarian cancer. *BMJ* **2015**, *351*, h4443.

(15) Daikoku, T.; Wang, D.; Tranguch, S.; Morrow, J. D.; Orsulic, S.; DuBois, R. N.; Dey, S. K. Cyclooxygenase-1 is a potential target for prevention and treatment of ovarian epithelial cancer. *Cancer Res.* **2005**, *65*, 3735–3744.

(16) Daikoku, T.; Tranguch, S.; Trofimova, I. N.; Dinulescu, D. M.; Jacks, T.; Nikitin, A. Y.; Connolly, D. C.; Dey, S. K. Cyclooxygenase-1 is overexpressed in multiple genetically engineered mouse models of epithelial ovarian cancer. *Cancer Res.* **2006**, *66*, 2527–2531.

(17) Lee, G.; Ng, H.-T. Clinical evaluations of a new ovarian cancer marker, COX-1. *Int. J. Gynaecol. Obstet.* **1995**, *49*, S27–S32.

(18) Sobolewski, C.; Cerella, C.; Dicato, M.; Ghibelli, L.; Diederich, M. The role of cyclooxygenase-2 in cell proliferation and cell death in human malignancies. *Int. J. Cell Biol.* **2010**, *2010*, 215158.

(19) Smith, W. L.; Urade, Y.; Jakobsson, P.-J. Enzymes of the cyclooxygenase pathways of prostanoid biosynthesis. *Chem. Rev.* **2011**, *111*, 5821–5865.

(20) Schneider, C.; Pozzi, A. Cyclooxygenases and lipoxygenases in cancer. *Cancer Metastasis Rev.* **2011**, *30*, 277–294.

(21) Wakabayashi, K. NSAIDs as Cancer Preventive Agents. *Asian Pac. J. Cancer Prev.* **2000**, *1*, 97–113.

(22) Wilson, A. J.; Fadare, O.; Beeghly-Fadiel, A.; Son, D. S.; Liu, Q.; Zhao, S.; Saskowski, J.; Uddin, M. J.; Daniel, C.; Crews, B.; Lehmann, B. D.; Pietenpol, J. A.; Crispens, M. A.; Marnett, L. J.; Khabele, D. Aberrant over-expression of COX-1 intersects multiple pro-tumorigenic pathways in high-grade serous ovarian cancer. *Oncotarget* **2015**, *6*, 21353–21368.

(23) Perrone, M. G.; Malerba, P.; Uddin, M. J.; Vitale, P.; Panella, A.; Crews, B. C.; Daniel, C. K.; Ghebreselasie, K.; Nickels, M.; Tantawy, M. N.; Manning, H. C.; Marnett, L. J.; Scilimati, A. PET radiotracer [18F]-P6 selectively targeting COX-1 as a novel biomarker in ovarian cancer: Preliminary investigation. *Eur. J. Med. Chem.* **2014**, *80*, 562–568.

(24) Uddin, M. J.; Crews, B. C.; Blobaum, A. L.; Kingsley, P. J.; Gorden, D. L.; McIntyre, J. O.; Matrisian, L. M.; Subbaramaiah, K.; Dannenberg, A. J.; Piston, D. W.; Marnett, L. J. Selective visualization of cyclooxygenase-2 in inflammation and cancer by targeted fluorescent imaging agents. *Cancer Res.* **2010**, *70*, 3618–3627.

(25) Saba, N. F.; Choi, M.; Muller, S.; Shin, H. J. C.; Tighiouart, M.; Papadimitrakopoulou, V. A.; El-Naggar, A. K.; Khuri, F. R.; Chen, Z. G.; Shin, D. M. Role of cyclooxygenase-2 in tumor progression and survival of head and neck squamous cell carcinoma. *Cancer Prev. Res.* **2009**, *2*, 823–829.

(26) Zweifel, B. S.; Davis, T. W.; Ornberg, R. L.; Masferrer, J. L. Direct evidence for a role of cyclooxygenase 2-derived prostaglandin E2 in human head and neck xenograft tumors. *Cancer Res.* **2002**, *62*, 6706–6711.

(27) Mathew, S. T.; Devi, S. G.; Prasanth, V. V.; Vinod, B. Efficacy and Safety of COX-2 Inhibitors in the Clinical Management of Arthritis: Mini Review. *ISRN Pharmacol.* **2011**, *2011*, 480291.

(28) Asiri, A. M.; Al-Youbi, A. O.; Faidallah, H. M.; Ng, S. W.; Tiekink, E. R. 4-(5-Phenyl-3-trifluoro-methyl-1H-pyrazol-1-yl)-benzene-sulfonamide. *Acta Crystallogr., Sect. E: Struct. Rep. Online* **2011**, *67*, o2424.

(29) Orlando, B. J.; Malkowski, M. G. Crystal structure of rofecoxib bound to human cyclooxygenase-2. *Acta Crystallogr., Sect. F: Struct. Biol. Commun.* **2016**, *72*, 772–776.

(30) Chang, C.-C.; Lee, W.-S.; Hsieh, H.-G.; Chuang, C.-L.; Huang, H.-C.; Lee, F.-Y.; Lee, S.-D. Selective cyclooxygenase inhibition by SC-560 improves hepatopulmonary syndrome in cirrhotic rats. *PLoS One* **2017**, *12*, No. e0179809.

(31) Smith, C. J.; Zhang, Y.; Koboldt, C. M.; Muhammad, J.; Zweifel, B. S.; Shaffer, A.; Talley, J. J.; Masferrer, J. L.; Seibert, K.; Isakson, P. C. Pharmacological analysis of cyclooxygenase-1 in inflammation. *Proc. Natl. Acad. Sci. U. S. A.* **1998**, *95*, 13313–13318.

(32) Li, W.; Ji, Z.-l.; Zhuo, G.-c.; Xu, R.-j.; Wang, J.; Jiang, H.-r. Effects of a selective cyclooxygenase-1 inhibitor in SKOV-3 ovarian carcinoma xenograft-bearing mice. *Med. Oncol.* **2010**, *27*, 98–104.

(33) Fujisaki, Y.; Kawamura, K.; Wang, W.-F.; Ishiwata, K.; Yamamoto, F.; Kuwano, T.; Ono, M.; Maeda, M. Radiosynthesis and in vivo evaluation of ¹¹C-labeled 1,5-diarylpyrazole derivatives for mapping cyclooxygenases. *Ann. Nucl. Med.* **2005**, *19*, 617–625.

(34) Teng, X. W.; Abu-Mellal, A. K.; Davies, N. M. Formulation dependent pharmacokinetics, bioavailability and renal toxicity of a selective cyclooxygenase-1 inhibitor SC-560 in the rat. *J. Pharm. Pharm. Sci.* **2003**, *6*, 205–210.

(35) Zhu, J.; Song, X.; Lin, H. P.; Young, D. C.; Yan, S.; Marquez, V. E.; Chen, C. S. Using cyclooxygenase-2 inhibitors as molecular platforms to develop a new class of apoptosis-inducing agents. *J. Natl. Cancer Inst.* **2002**, *94*, 1745–1757.

(36) Uddin, M. J.; Elleman, A. V.; Ghebreselasie, K.; Daniel, C. K.; Crews, B. C.; Nance, K. D.; Huda, T.; Marnett, L. J. Design of Fluorine-Containing 3,4-Diarylfuran-2(SH)-ones as Selective COX-1 Inhibitors. *ACS Med. Chem. Lett.* **2014**, *5*, 1254–1258.

(37) de Vries, E. F. J.; Doorduyn, J.; Dierckx, R. A.; van Waarde, A. Evaluation of [¹¹C]rofecoxib as PET tracer for cyclooxygenase 2 overexpression in rat models of inflammation. *Nucl. Med. Biol.* **2008**, *35*, 35–42.

(38) Wüst, F. R.; Höhne, A.; Metz, P. Synthesis of ¹⁸F-labelled cyclooxygenase-2 (COX-2) inhibitors via Stille reaction with 4-[¹⁸F]fluoriodobenzene as radiotracers for positron emission tomography (PET). *Org. Biomol. Chem.* **2005**, *3*, 503–507.

(39) Kumar, A.; Mann, S.; Sossi, V.; Ruth, T. J.; Stoessl, A. J.; Schulzer, M.; Lee, C. S. [¹¹C]DTBZ-PET correlates of levodopa responses in asymmetric Parkinson's disease. *Brain* **2003**, *126*, 2648–2655.

(40) Liu, Z.; Yang, Z.; Yu, X.; Zhang, H.; Yu, B.; Zhao, Y.; Liu, Z. Methylation of C(sp³)-H/C(sp²)-H Bonds with Methanol Catalyzed by Cobalt System. *Org. Lett.* **2017**, *19*, 5228–5231.

(41) Chaudhari, M. B.; Sutar, Y.; Malpathak, S.; Hazra, A.; Gnanaprakasam, B. Transition-Metal-Free C-H Hydroxylation of Carbonyl Compounds. *Org. Lett.* **2017**, *19*, 3628–3631.

(42) Hayashi, Y.; Yamaguchi, J.; Sumiya, T.; Hibino, K.; Shoji, M. Direct Proline-Catalyzed Asymmetric α -Aminooxylation of Aldehydes and Ketones. *J. Org. Chem.* **2004**, *69*, 5966–5973.

(43) Pacifici, G. M.; Viani, A. Methods of Determining Plasma and Tissue Binding of Drugs. *Clin. Pharmacokinet.* **1992**, *23*, 449–468.